ADVANCED MATERIALS INTERFACES
www.advmatinterfaces.de

Cryogenic Temperature Growth of Sn Thin Films on Ferromagnetic Co(0001)

Leszek Gładczuk, Łukasz Gładczuk, Piotr Dłużewski, Pavlo Aleshkevych, Artem Lynnyk, Gerrit van der Laan,* and Thorsten Hesjedal**

Topological electronic materials hold great promise for revolutionizing spintronics, owing to their topological protected, spin-polarized conduction edge or surface state. One of the key bottlenecks for the practical use of common binary and ternary topological insulator materials is the large defect concentration that leads to a high background carrier concentration. Elemental tin in its α-phase is a room temperature topological semimetal, which is intrinsically less prone to defect-related shortcomings. Recently, the growth of ultrathin α-Sn films on ferromagnetic Co surfaces has been achieved; however, thicker films are needed to reach the 3D topological Dirac semimetallic state. Here, the growth of α-Sn films on Co at cryogenic temperatures was explored. Very low-temperature growth holds the promise of suppressing undesired phases, alloying across the interfaces, as well as the formation of Sn pillars or hillocks. Nevertheless, the critical Sn layer thickness of ≈3 atomic layers, above which the film partially transforms into the undesired β-phase, remains the same as for room-temperature growth. From ferromagnetic resonance studies, and supported by electron microscopy, it can be concluded that for cryogenic Sn layer growth, the interface between Sn and Co remains sharp and the magnetic properties of the Co layer stay intact.

1. Introduction

Topological insulators (TIs) are a class of materials that is insulating in the bulk and conducting at the surface.[1] They are known for the protection of their topological surface state against backscattering by time-reversal symmetry (TRS), full spin-polarization, very high carrier mobility, and low energy dissipation.[2–9] So far, all experimentally confirmed binary or ternary topological Dirac materials have the intrinsic problem of defect–induced bulk conductivity,[10] whereas elemental materials provide in general a more promising route for suppressing undesired defect contributions.

Interfaces are key to TIs, as the combination of materials with different topological band character are the origin of the formation of topological surface or edge states in the first place. The breaking of TRS via interface engineering, i.e., via the interface with a magnetically ordered system,[11–13] is the key requirement for achieving the quantum anomalous Hall state.[14] Of more practical importance, however, is the observation that carriers in a TI can exert significant spin torque on an exchange-coupled ferromagnetic layer,[15] enabling all-electrical switching of the magnetic layer. Another important effect that has been demonstrated in TIs is spin pumping,[16,17] i.e., the injection of a pure spin (and not charge) current from a ferromagnetic layer undergoing ferromagnetic resonance into an adjacent layer.[18] Spin pumping in TIs,[19,20] which forms the basis of TI-based spin-valve structures, was reported earlier.[21] One convenient way for studying spin pumping is to analyze the broadening of the magnetic resonance absorption of the pumping ferromagnetic layer at resonance. A larger pumped spin current will lead to additional damping, and thus broadening of the resonance, which is captured by an extra term in the magnetodynamic equations.[22]

Elemental tin (Sn) has two crystallographic phases, α-Sn (gray tin) and β-Sn (white tin), with the α-phase being stable below 13.2 °C. The high-temperature β-phase has a tetragonal crystal structure and is metallic, while gray tin has a diamond crystal structure (6.467 Å) and is classified as a semimetal with a direct band gap of 0 eV, and a "negative" band gap of $\Gamma_7 - \Gamma_8 = -0.413$ eV.[23] Application of uniaxial stress makes α-Sn a semiconductor as it splits the degenerate Γ_8 state.[24] Due to its

L. Gładczuk, P. Dłużewski, P. Aleshkevych, A. Lynnyk
Institute of Physics
Polish Academy of Science
Aleja Lotnikow 32/46, Warsaw PL-02668, Poland
E-mail: gladl@ifpan.edu.pl
Ł. Gładczuk, T. Hesjedal
Department of Physics
Clarendon Laboratory
University of Oxford
Oxford OX1 3PU, UK
E-mail: thorsten.hesjedal@physics.ox.ac.uk
G. van der Laan
Diamond Light Source
Harwell Science and Innovation Campus
Didcot, Oxfordshire OX11 0DE, UK
E-mail: gerrit.vanderlaan@diamond.ac.uk

The ORCID identification number(s) for the author(s) of this article can be found under https://doi.org/10.1002/admi.202201452.

DOI: 10.1002/admi.202201452

simple structure compared to binary or ternary materials, Sn has the potential to show lower defect densities—and thus suppress the unwanted bulk conductivity. Owing to its strain and dimensionality dependent topological properties, α-Sn is a versatile platform for exploring exotic electronic effects.[25] For this very reason, α-Sn has recently received a lot of attention, reports can be found of gray tin stabilized on InSb(111)[26] or In-terminated InSb(111)A,[27] with the α-β transition temperature reaching as high as 170°C.[28] Recently, the efficient charge-to-spin conversion with spin–orbit torque efficiencies comparable to Pt have been demonstrated in a clean Sn-ferromagnet system, i.e., FeCo/Sn/CdTe,[29] as well as before in the more complex Fe/Ag/Bi/Sn/ substrate heterostructure.[30] This breakthrough demonstration of the the promise of α-Sn for spintronic devices relied on epitaxially grown α-Sn films on CdTe(001), which were then covered with the ferromagnetic layer. Although some studies of α-Sn/ferromagnet interface properties have been conducted[31] it remains a challenge to grow α-Sn on top of a ferromagnetic material, i.e., the inverse interface, which is crucial for opening the door for more complex device structures such as spin-valves.[32] Recently, we have shown that strained α-Sn can be stabilized on hcp Co(0001) surfaces;[33] however, owing to the comparably low film quality, no unambiguous proof for spin pumping through a ferromagnet-Sn-ferromagnet spin valve structure was given.

Sn segregation is a common problem in heterostructure growth involving Sn, and it has been intensely investigated in the context of Sn/Ge.[34] The growth at cryogenic substrate temperatures, also involving low growth rates, opens up the possibility to obtain α-Sn in conditions far beyond the thermodynamic equilibrium. In fact, in the seminal work by Farrow et al.,[35] in which epitaxial α-Sn growth on InSb and CdTe was reported for the first time, a substrate temperature of –20°C was chosen; however, due to the heat from the Sn effusion cell, the temperature increased to 25°C during growth. Apart from thermodynamic reasons, slightly elevated temperatures have been reported to lead to diffusion from the InSb substrate, accompanied by increased surface roughness.[36] In our first demonstration of α-Sn growth on a ferromagnet,[33] we noted an improvement of the film quality with decreasing temperature. Unfortunately, the temperature range below 25°C (during growth, with the effusion cell shutters open) is not accessible in a standard MBE system.

Here, we explore the cryogenic-temperature growth of Sn on hcp Co(0001) by molecular beam epitaxy, and study the magnetization dynamics across the Sn/Co interface with ferromagnetic resonance (FMR). We use cross-sectional transmission electron microscopy (XTEM) to understand the microstructure of the Sn layer for different growth conditions and at different stages of the growth. We find that Sn initially forms strained, uniform layers in the ultrathin limit, while droplets (or pillars) form beyond a few atomic layers. We used FMR to study the magnetization dynamics of the Sn/Co system, in comparison with MgO/Co and Au/Co, and determined the anisotropy constants of the Co layer. We find a relatively low damping in the ultrathin limit, while with increasing Sn thickness the damping increases significantly. This increase in damping is caused by the polycrystalline character of the thicker Sn layers, due to the relaxation of strain imposed by the underlying Co layer. Our combined FMR and XTEM study shows that for cryogenic growth, high-quality strained Sn layers can be obtained up to a thickness of ≈3 atomic layers.

2. Sample Preparation and Characterization

The growth of Sn thin films has been achieved on a number of substrates, including Si[37–41] and Ge.[42–45] The stabilization of the α-phase up to high temperatures has been reported for the near-lattice-matched substrates InSb(001)[46,47] and Sb-terminated InSb(111)B.[26,48] Recently, we reported the successful growth of α-Sn on magnetic, hexagonal closed-packed (hcp) Co(0001) up to a thickness of a few atomic layers.[33] In this study, we found promising hints for a possible route for achieving thicker, phase-pure α-Sn films, i.e., the growth at cryogenic temperatures.

Here, we have adopted a similar approach as presented in Ref. [33]. A Mo/Au/Al_2O_3 heterostructure template[49] was used as a virtual substrate for hcp Co(0001) growth. Subsequently, a 0.8–5 nm thick Co layer was deposited, while monitoring its quality during growth using reflection high-energy electron diffraction (RHEED). Finally, a Sn layer of up to 5 nm in thickness was deposited on top of the Co layer, again, monitoring its quality with RHEED. Representative RHEED images, taken for Co(0001) hexagonal basal plane and at the various stages of the Sn growth, are shown in **Figure 1**. The RHEED images of the Co(0001) layer present two distinct symmetry axes rotated azimuthally by 30°. During the Sn growth process, the substrate temperature was kept at ≈–50 °C. This temperature prevents the formation of CoSn alloys. The Sn effusion cell was kept at ≈1050 °C achieving a deposition rate of 0.02 nm s^{-1}. Deposition of 0.12 nm of Sn onto the Co(0001) surface blurs the streaks, while their position remains the same. A new crystallographic surface structure emerges when the Sn layer reaches a thickness of 0.9 nm. The atomic distance is 0.443 nm (at 5° azimuth), i.e., twice of the distance observed for Co in the RHEED image along the 30° azimuth. In order to understand the spin pumping in this Sn/Co interfacial system, three more heterostructures were grown for comparison with the identical Co thickness, i.e., a thin Sn layer system (Au/MgO/Sn/Co), and a conductive Au/Co and an insulating MgO/Co system.

The grown samples were then characterized using XTEM with energy-dispersive spectroscopy (EDS) analysis to determine the crystal structure, elemental distribution, and morphological properties. Using XTEM with EDS analysis, we confirmed the quality of the Co layer and studied the interfacial region between the Co and the Sn layers (see **Figures 2–4**). The Sn growth on Co proceeds via the Stranski–Krastanov growth mechanism. Thin Sn layers on Co are initially flat, up to a thickness of three monolayers, before the growth mode changes. The interplanar distance of this layers does not match that of either α-Sn nor β-Sn. It is possible that the Sn layer is highly strained due to the underlying Co film. When the Sn growth is continued beyond the critical thickness, Sn droplets begin to form. These droplets have a tetragonal crystal structure, in agreement with β–Sn.

The magnetic properties of the samples were studied by carrying out FMR measurements at room temperature with a conventional X-band Bruker EMX spectrometer. The samples were mounted on a quartz sample holder and placed in a cavity. The FMR spectra were recorded as a function of the orientation of an applied DC external magnetic field from 0 to 1.6 T.

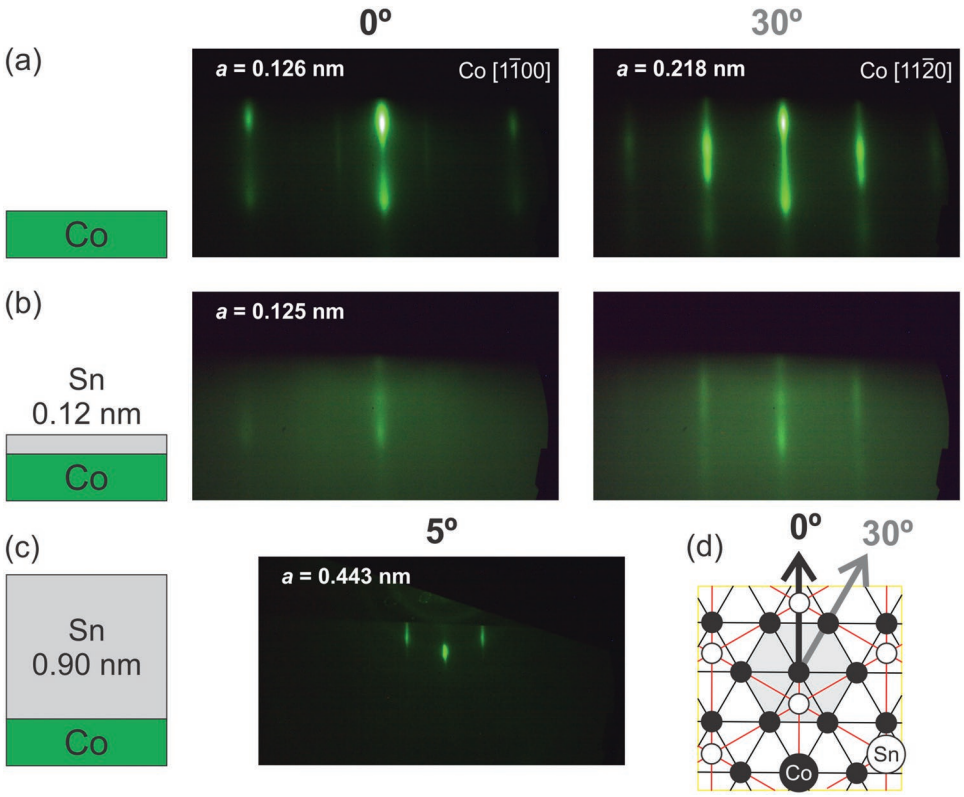

Figure 1. RHEED images taken on a) the Co surface prior to Sn growth, and b) after 0.12 nm and c) 0.90 nm of Sn growth, along the 0°, 5°, and 30° azimuths as indicated. d) Illustration of the azimuthal orientations in the hexagonal Co(0001) basal plane. A possible configuration of the Sn layer (white circles) on the Co surface (black circles) is illustrated. For details see Ref. [33].

3. Modeling and Data Analysis

The cavity FMR measurements were performed at a fixed frequency of 9.38 GHz as a function of the applied magnetic field (H_0) and field orientation (θ_H) in a plane perpendicular to the sample surface. The radio frequency (RF) field exciting the resonance is applied perpendicular to the DC magnetic field. The experimental results were fitted with the theoretical predictions

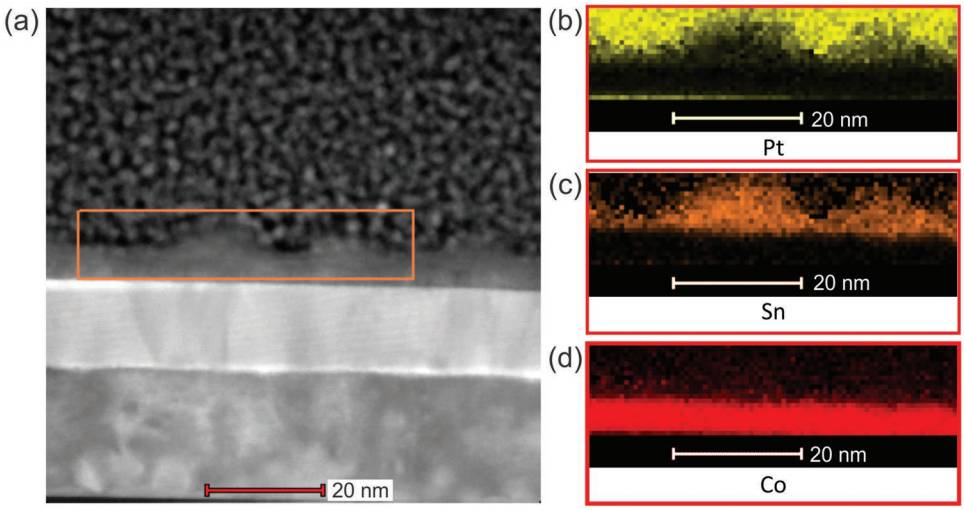

Figure 2. a) STEM/HAADF image of a nominally 4-nm-thick Sn film deposited onto a (111)-oriented Co layer. The orange rectangle indicates the area in which the elemental EDS maps, shown at the right hand side for d) Co and c) Sn, as well as b) the Pt layer (added for protecting the layer stack before ion milling), were taken. An abrupt interface between Co and the continuous Sn can be seen. The thick Sn layer is rough and shows clear pillar structures.

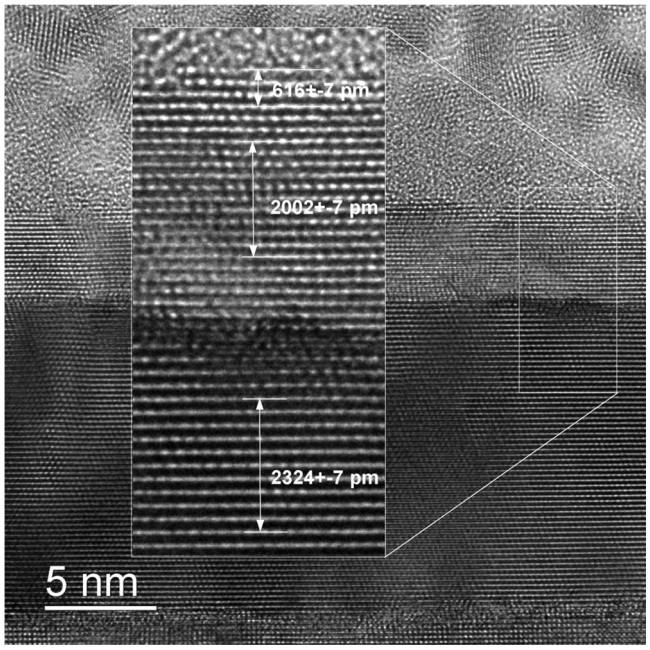

Figure 3. High-resolution TEM image of the top part of a Sn(3-4 monolayer)/Co/Au/Mo/Al_2O_3 heterostructure. The interplanar spacings for the Au, Co, and Sn layers (from bottom to top) are indicated in the inset, ranging from 235 pm for the Au(111) layer, to 203 pm for Co(111) layer, and finally 208 pm for the Sn layer.

obtained using the Landau–Lifshitz–Gilbert (LLG) equation, allowing for the extraction of the anisotropy constants and the Gilbert damping coefficient.

For the purpose of this study, the anisotropy of the Co layer was assumed to be uniaxial, with the anisotropy axis oriented perpendicular to the sample plane. The anisotropy energy was approximated using two coefficients (K_1, K_2)[50]

$$E_a(\theta) = K_1 \sin^2\theta + K_2 \sin^4\theta \tag{1}$$

When the sample is placed in the external magnetic field, both the magnetic field and the sample anisotropy affect the magnetization of the sample (**M**). The resulting orientation of the sample magnetization (θ) is found by solving Brown's equations, which in the present case takes the form, Ref. [51]

$$\mu_0 H_{\text{ext}} \sin(\theta - \theta_H) + D_1 \cos\theta \sin\theta + D_2 \cos^3\theta \sin\theta = 0 \tag{2}$$

where $D_1 = 2(K_1^{\text{eff}} + 2K_2)/M_s$ and $D_2 = -4K_2/M_s$, where M_s is the saturation magnetization. Here, the shape anisotropy has been incorporated into the effective anisotropy coefficient $K_1^{\text{eff}} = K_1 - \mu_0 M_s^2/2$. In the calculations, we assumed the saturation magnetization of the Co layer to be 1.44×10^6 A/m.[52]

The dynamic spin precession can be described by solving the LLG equation

$$\frac{\partial \mathbf{m}}{\partial t} = -\gamma \mathbf{m} \times \mathbf{H}_{\text{eff}}(\mathbf{m}) + \alpha \mathbf{m} \times \frac{\partial \mathbf{m}}{\partial t} \tag{3}$$

where $\mathbf{m} = \mathbf{M}/M_s$ is the unit vector in the direction of magnetization, α is the Gilbert damping coefficient, and $\mathbf{H}_{\text{eff}}$ is the effective magnetic field, composed of $\mathbf{H}_0$, the magnetic RF field, and the anisotropy field. By knowing the dynamics of the magnetization vector, the energy dissipation, as measured by the FMR experiment, is found by evaluating

$$I = \mu_0 \left\langle \mathbf{M} \cdot \frac{d}{dt} \mathbf{H}_{\text{eff}} \right\rangle \tag{4}$$

where $\langle\rangle$ denotes the time average. The detailed derivation of the above equations, as well their solutions, can be found in Ref. [51].

In principle, the sample properties K_1, K_2, and α are obtained by fitting the theoretical curve to the measured FMR data. In practice, however, such fits are not perfect due to undesired contributions of, e.g., the sample holder. Therefore, we adopted the following methodology: First, a Lorentzian function of the form (together with its Kramers–Kronig relationship counterpart)

$$f(H) = \frac{A_1}{\pi} \frac{\Delta H/2}{(H - H_0)^2 + (\Delta H/2)^2} + \frac{A_2}{\pi} \frac{H - H_0}{(H - H_0)^2 + (\Delta H/2)^2} + A_3 + A_4 H + A_5 H^2 \tag{5}$$

is fitted to the raw FMR data, and the resonance magnetic field (H_0) and half-width at full maximum (FWHM) (ΔH) of the resonance peak are determined, and compared to the theoretical values. The coefficients A_3, A_4, and A_5 are introduced to correct for the background signal. We define H_0 as the field maximizing the absorption in Equation (4).

Figure 5 shows a comparison between the theoretical FMR curve derived from Equation (4) and fits based on a Lorentzian function using Equation (5). The Lorentzian function describes the shape of the experimental FMR signal better, and allows for

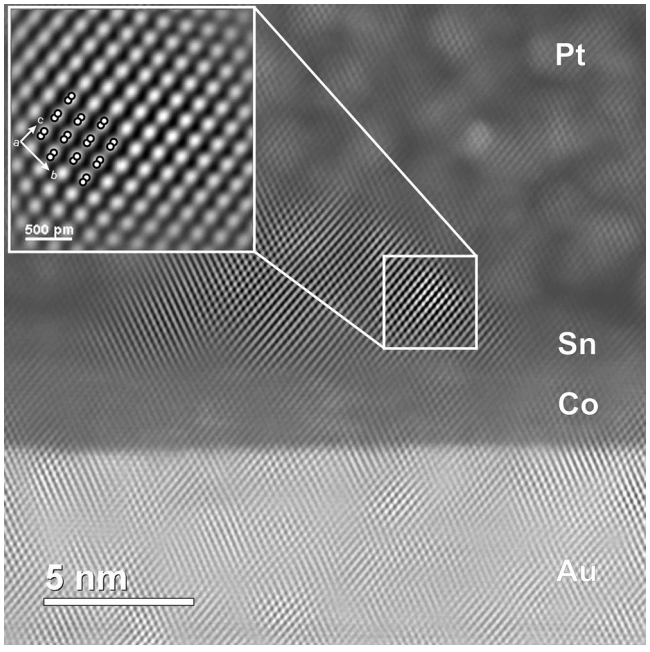

Figure 4. High-resolution TEM image of a thick Sn layer, showing the formation of the β-phase in the extruding pillars. The inset shows a contrast-enhanced enlargement of the area indicated by the white square.

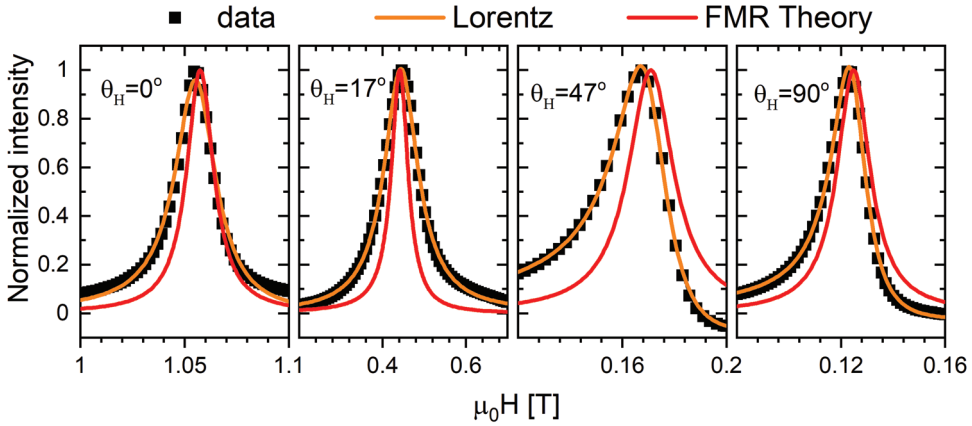

Figure 5. FMR absorption signal for a Sn(5 nm)/Co(4 nm) sample as a function of the external magnetic field strength for a field orientation of $\theta_H = 0°$, $\theta_H = 17°$, $\theta_H = 47°$, $\theta_H = 90°$. The data shown in the figure was normalized by their respective maxima. The orange curve represents the fit obtained using the Lorentz function [Equation (5)], and the red curve represents the theoretical FMR signal (Equation (4)), derived from the LLG Equation (3). Parameters for the FMR theory were obtained from model fittings shown in Figures 6a and 6b.

the extraction of ΔH and H_0, even if the signal is affected by effects not included in the theoretical model.

Figure 6a shows plots of the magnetic resonance field as a function of field angle for uncapped and capped Sn/Co heterostructures, as well as reference samples in which Sn has been replaced by Au. From fitting the experimental values (solid circles), the anisotropy constants K_1 and K_2 were extracted. Figure 6b shows plots of the measured (and fitted) ΔH values (FWHM) for the four different interfaces, from which the damping constant α was obtained. The angular dependence of the resonance field is very similar for Sn/Co and the three reference systems (with the same Co layer thickness), see Figure 6a. On the other hand, the ΔH values, shown in Figure 6b, are markedly different. The Au/MgO/Co sample shows the lowest damping ($\alpha_{MgO} = 0.016$), and the theoretical model describes the experimentally observed angular dependence of ΔH very well. On the other hand, Au/Co shows the highest damping ($\alpha_{Au} = 0.03$), and the theoretical model captures the experimental $\Delta H(\theta_H)$ data over a wide angular range, except for small θ_H values. In general, we observe a discrepancy between theory and experiment for field directions close to the hard axis direction, as in the case of Au/Co for small θ_H. This behavior is likely due to the interaction between multiple magnetic domains, which may be present in the sample due to crystallographic imperfections. Our single domain model, used here, is thus not able to capture these effects. For a more detailed discussion, we refer to Ref. [51].

A very different behavior is observed for the Sn/Co sample. For low and high values of θ_H, ΔH is similar to the behavior of the MgO/Co sample. However, at ≈15°, a large deviation of the experimental data from the theoretically expected behavior is observed, whereby the experimentally observed damping greatly exceeds the expected values (compare blue circles and line in Figure 6b). To understand this discrepancy, we measured a MgO/Sn/Co structure in which the Co thickness was kept the same; however, the Sn thickness was 0.8 nm and thus less than the critical value. Finally, an MgO layer was added to keep the overall thickness of the layer stack the same for both samples. For MgO/Sn/Co (orange circles and line in Figure 6b), theory and experiment closely match, giving $\alpha_{Sn} = 0.014$. This damping value is close to one obtained for the Au/MgO/Co sample, and much smaller than for Au/Co. The observed large damping in the 4-nm-thick Sn layer is therefore most likely due to the presence of β-Sn pillars in the layer. Such structural imperfections create variations in sample properties, which can promote the creation

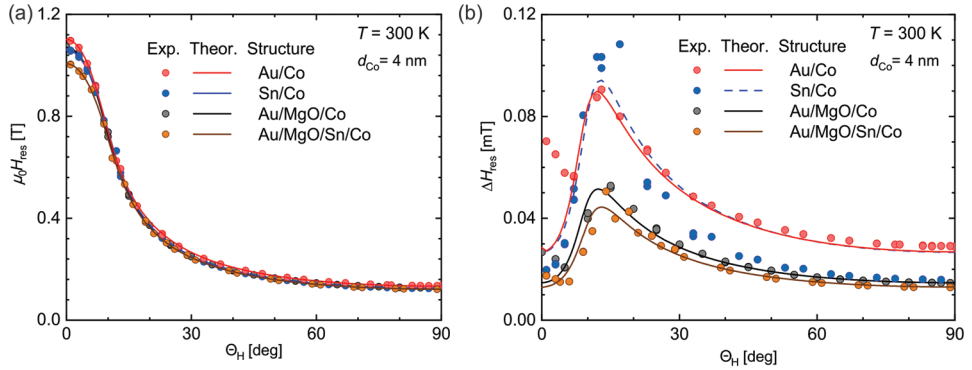

Figure 6. Experimental results and theoretical fits of: a) resonance magnetic field and b) resonance half-width for samples of Au(cap)/MgO(4)/Co(4), Sn(4)/Co(4), Au(4)/Co(4), and Au(cap)/MgO(3)/Sn(0.8)/Co(4) (thicknesses in nm).

Table 1. Summary of the magnetic sample parameters obtained by fitting the experimental FMR data.

sample	γ [m/(s· A)]	$-D_1$ [mT]	$-D_2$ [mT]	K_1 [10^3 A/m]	$K_\uparrow^{eff}$ [10^3 A/m]	K_2 [10^3 A/m]	α [10^{-3}]
Au/Co	224 100 ± 300	684 ± 3	86.2 ± 4	748 ± 3	−555 ± 2	31 ± 1	28.0 ± 1.0
Sn/Co	229 500 ± 800	711 ± 1	27 ± 11	772 ± 10	−531 ± 6	10 ± 4	29.4 ± 1.6
Au/MgO/Co	230 800 ± 600	696 ± 7	53.2 ± 8	763 ± 8	−539 ± 4	19 ± 3	16.6 ± 0.3
Au/MgO/Sn/Co	239 700 ± 500	664 ± 6	33 ± 6	801 ± 6	−502 ± 3	12 ± 2	14.2 ± 0.3

of domain walls, and thus increase damping. **Table 1** summarizes the magnetic parameters of all samples.

Next, we investigated the thickness dependence of the Co anisotropy in the Sn/Co structure (**Figure 7**). For d_{Co} in the range between 1.7 and 4.8 nm, we determined both K_1 and K_2. Figure 7 shows the thickness dependence of the dominant K_1^{eff} parameter for the Sn/Co structure (solid circles), and, in comparison, for Au/Co structures (open circles). The effect of the interface on the Co anisotropy can be modeled as

$$K_1^{eff}(d_{Co}) = K_1^{eff}(\infty) + K_s/d_{Co} \quad (6)$$

where K_s is the surface anisotropy, and $K_1^{eff}(\infty)$ is the anisotropy of the bulk crystal. K_1^{eff} is negative for thick samples ($d_{Co} > 1.90$ nm), i.e., the sample magnetization favors to be in-plane. For thin samples ($d_{Co} < 1.90$ nm), K_1^{eff} is positive, i.e., the sample magnetization favors to be perpendicular to the surface. The comparison with a series of Au/Co samples[53] shows that their behavior is very similar, i.e., the effect of the Sn layer on the anisotropy of the Co layer is small. We can therefore conclude that the cryogenic-temperature growth of Sn is not affecting the magnetic properties of the Co layer, most likely due to the suppression of interfacial reactions, which could lead to the formation of CoSn alloys.

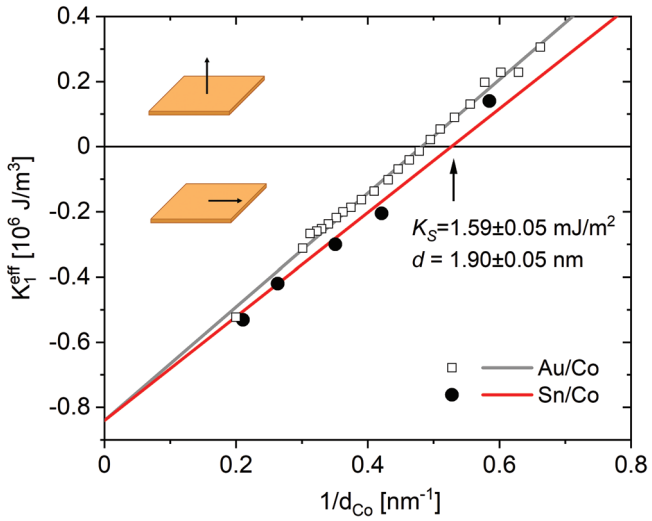

Figure 7. Effective anisotropy coefficient $K_\uparrow^{eff}$ of the Co layer as a function of the inverse of the Co layer thickness (d_{Co}) for a Sn layer thickness of 1.2 nm. For large Co layer thicknesses (>1.90 nm), $K_\uparrow^{eff}$ is negative, i.e., the Co layer shows in-plane anisotropy. For thin Co layers (<1.90 nm), $K_\uparrow^{eff}$ is positive, i.e., the Co layer shows perpendicular magnetic anisotropy. In total, five different Co thicknesses were measured for the Sn/Co system. The data for the Sn/Co system (solid circles and red line) are compared with the experimental results obtained for Au/Co samples (open squares and black line), published in Ref. [53].

4. Conclusion

In summary, we have studied the cryogenic-temperature growth of Sn layers on hcp Co(0001) up to a Sn layer thickness of 5 nm. Up to a thickness of ≈3 atomic layers, strained, flat Sn layers are found. Above that critical thickness, the layer roughens and contributions from β-Sn are observed, forming pillars. Thin Sn layers are strained via the constraints imposed by the underlying Co layer. However, due to its low thickness, we are not able to unambiguously determine its crystallographic structure. As a next step, it is important to study the effects of the strain on the electronic bandstructure of the films by carrying out angle-resolved photoemission spectroscopy measurements.

The magnetic properties of the underlying Co layer were not detrimentally affected by the Sn layer, and its effect on the Co anisotropy is similar to commonly used MgO or Au capping layers. By comparing the anisotropy constant K_1^{eff} for Co in thick Sn/Co and Au/Co interface systems, we found a similar strong coupling between the magnetic and nonmagnetic layers. For thin Sn layers, on the other hand, the damping was the lowest out of all studied samples, and close to the case of Co covered with MgO.

5. Experimental Section

Thin Film Growth: All samples were grown by molecular beam epitaxy (MBE) at the Institute of Physics, Polish Academy of Sciences (Warsaw, Poland). For the growth of the hcp Co(0001) layer, Au/Mo/Al_2O_3 heterostructure templates were used as a virtual substrate. The Co layer was grown at room temperature and at a deposition rate of 0.016 nm s^{-1}. The sample temperature was then lowered to ≈−50°C and kept for the remainder of the deposition process. For cooling the sample, the sample holder was brought into contact with an Al plate that was extending from the cryoshroud. Due to the relatively large thermal mass of the cryoshroud, this plate had a relatively constant temperature of ≈−140°C, resulting in a sample temperature of ≈−50°C (as determined by a type K thermocouple calibration). Next, a 0–5 nm thick Sn film was grown. To assure that the sample temperature did not increase due to the direct heat from the Sn cell, the growth was interrupted after 1 min for 10 min, before continuing with this sequence until the desired thickness was reached. The samples were then capped with either Au or 4 nm of MgO, followed by Au. The films were structurally characterized in-situ using reflection high-energy electron diffraction (RHEED). The interface and crystalline quality of the heterostructures was investigated using cross-sectional transmission electron microscopy (XTEM), equipped with an energy-dispersive spectroscopy (EDS) detector. The magnetic properties were studied using ferromagnetic resonance (FMR) and superconducting quantum interference device (SQUID) magnetometry.

Statistical Analysis: 1) The data presented in Figure 5 was was normalized to their respective maxima. 2) The mean values and standard deviations are given for the relevant fits (Figure 6b) in Table 1. 3) The number of data points in each of the FMR spectra is ≈4000, and the number of field-dependent spectra measured for each sample varies (Au/Co: 66; Sn/Co: 31 ; Au/MgO/Co: 40; and Co/Sn/MgO/Au: 30 measurement points). In total five different thickness were measured for Sn/Co sample (Figure 7). 4) No statistical methods were employed to test the hypotheses in this work. 5) The magnetic parameters extracted from fitting the model (Equation (5)) to the data, as well as the uncertainties, were found as maximum likelihood estimators, using the "NonlinearModelFit" method as implemented in the software package Mathematica (v12.1). A custom Monte Carlo algorithm was used to estimate the uncertainty of the Gilbert damping parameter α, as in this case the use of the built-in methods in Mathematica were computationally not efficient. The Monte Carlo method is similar to one described in Section VI of Ref. [54].

Acknowledgements

Ł.G. was supported through a joint studentship between the Diamond Light Source and the University of Oxford (support by Engineering and Physical Sciences Research Council through a doctoral training award).

Conflict of Interest

The authors declare no conflict of interest.

Data Availability Statement

The data that support the findings of this study are available from the corresponding author upon reasonable request.

Keywords

ferromagnetic resonance, spin pumping, topological insulators, topological quantum materials

Received: July 1, 2022
Revised: October 3, 2022
Published online: October 26, 2022

[1] J. E. Moore, *Nature* **2010**, *464*, 194.
[2] L. Fu, C. L. Kane, E. J. Mele, *Phys. Rev. Lett.* **2007**, *98*, 106803.
[3] C. L. Kane, E. J. Mele, *Phys. Rev. Lett.* **2005**, *95*, 146802.
[4] B. A. Bernevig, T. L. Hughes, S.-C. Zhang, *Science* **2006**, *314*, 1757.
[5] J. E. Moore, L. Balents, *Phys. Rev. B* **2007**, *75*, 121306.
[6] R. Roy, *Phys. Rev. B* **2009**, *79*, 195322.
[7] Y. L. Chen, J. G. Analytis, J.-H. Chu, Z. K. Liu, S.-K. Mo, X. L. Qi, H. J. Zhang, D. H. Lu, X. Dai, Z. Fang, S. C. Zhang, I. R. Fisher, Z. Hussain, Z.-X. Shen, *Science* **2009**, *325*, 178.
[8] Y. L. Chen, J. H. Chu, J. G. Analytis, Z. K. Liu, K. Igarashi, H. H. Kuo, X. L. Qi, S. K. Mo, R. G. Moore, D. H. Lu, M. Hashimoto, T. Sasagawa, S. C. Zhang, I. R. Fisher, Z. Hussain, Z. X. Shen, *Science* **2010**, *329*, 659.
[9] D. Kong, Y. Cui, *Nat. Chem.* **2011**, *3*, 845.
[10] S. S. Hong, J. J. Cha, D. Kong, Y. Cui, *Nat. Commun.* **2012**, *3*, 757.
[11] M. Z. Hasan, C. L. Kane, *Rev. Mod. Phys.* **2010**, *82*, 3045.
[12] M. R. Scholz, J. Sánchez-Barriga, D. Marchenko, A. Varykhalov, A. Volykhov, L. V. Yashina, O. Rader, *Phys. Rev. Lett.* **2012**, *108*, 256810.
[13] L. A. Wray, S.-Y. Xu, Y. Xia, D. Hsieh, A. V. Fedorov, Y. S. Hor, R. J. Cava, A. Bansil, H. Lin, M. Z. Hasan, *Nat. Phys.* **2011**, *7*, 32.
[14] C.-Z. Chang, J. Zhang, X. Feng, J. Shen, Z. Zhang, M. Guo, K. Li, Y. Ou, P. Wei, L.-L. Wang, Z.-Q. Ji, Y. Feng, S. Ji, X. Chen, J. Jia, X. Dai, Z. Fang, S.-C. Zhang, K. He, Y. Wang, L. Lu, X.-C. Ma, Q.-K. Xue, *Science* **2013**, *340*, 167.
[15] T. Yokoyama, J. Zang, N. Nagaosa, *Phys. Rev. B* **2010**, *82*, 241410(R).
[16] Y. Tserkovnyak, A. Brataas, G. E. W. Bauer, B. I. Halperin, *Rev. Mod. Phys.* **2005**, *77*, 1375.
[17] B. Heinrich, Y. Tserkovnyak, G. Woltersdorf, A. Brataas, R. Urban, G. E. W. Bauer, *Phys. Rev. Lett.* **2003**, *90*, 187601.
[18] A. Brataas, Y. Tserkovnyak, G. E. W. Bauer, B. I. Halperin, *Phys. Rev. B* **2002**, *66*, 060404.
[19] J. Tian, I. Childres, H. Cao, T. Shen, I. Miotkowski, Y. P. Chen, *Solid State Commun.* **2014**, *191*, 1.
[20] A. R. Mellnik, J. S. Lee, A. Richardella, J. L. Grab, P. J. Mintun, M. H. Fischer, A. Vaezi, A. Manchon, E.-A. Kim, N. Samarth, D. C. Ralph, *Nature* **2014**, *511*, 449.
[21] A. A. Baker, A. I. Figueroa, L. J. Collins-McIntyre, G. van der Laan, T. Hesjedal, *Sci. Rep.* **2015**, *5*, 7907.
[22] Y. Tserkovnyak, A. Brataas, G. E. W. Bauer, *Phys. Rev. B* **2002**, *66*, 224403.
[23] O. Madelung, *Semiconductors: Data Handbook*, Springer, Berlin, Heidelberg **2004**.
[24] M. Cardona, *Solid State Commun.* **1967**, *5*, 233.
[25] Q. Barbedienne, J. Varignon, N. Reyren, A. Marty, C. Vergnaud, M. Jamet, C. Gomez-Carbonell, A. Lemaître, P. Le Fèvre, F. M. C. Bertran, A. Taleb-Ibrahimi, H. Jaffrès, J.-M. George, A. Fert, *Phys. Rev. B* **2018**, *98*, 195445.
[26] C.-Z. Xu, Y.-H. Chan, Y. Chen, P. Chen, X. Wang, C. Dejoie, M.-H. Wong, J. A. Hlevyack, H. Ryu, H.-Y. Kee, N. Tamura, M.-Y. Chou, Z. Hussain, S.-K. Mo, T.-C. Chiang, *Phys. Rev. Lett.* **2017**, *118*, 146402.
[27] V. A. Rogalev, F. Reis, F. Adler, M. Bauernfeind, J. Erhardt, A. Kowalewski, M. R. Scholz, L. Dudy, L. B. Duffy, T. Hesjedal, M. Hoesch, G. Bihlmayer, J. Schäfer, R. Claessen, *Phys. Rev. B* **2019**, *100*, 245144.
[28] H. Song, J. Yao, Y. Ding, Y. Gu, Y. Deng, M.-H. Lu, H. Lu, Y.-F. Chen, *Adv. Eng. Mater.* **2019**, *21*, 1900410.
[29] F. Binda, C. O. Avci, S. F. Alvarado, P. Noël, C.-H. Lambert, P. Gambardella, *Phys. Rev. B* **2021**, *103*, 224428.
[30] J.-C. Rojas-Sánchez, S. Oyarzún, Y. Fu, A. Marty, C. Vergnaud, S. Gambarelli, L. Vila, M. Jamet, Y. Ohtsubo, A. Taleb-Ibrahimi, P. Le Fèvre, F. Bertran, N. Reyren, J.-M. George, A. Fert, *Phys. Rev. Lett.* **2016**, *116*, 096602.
[31] M. R. Scholz, V. A. Rogalev, L. Dudy, F. Reis, F. Adler, J. Aulbach, L. J. Collins-McIntyre, L. B. Duffy, H. F. Yang, Y. L. Chen, T. Hesjedal, Z. K. Liu, M. Hoesch, S. Muff, J. H. Dil, J. Schäfer, R. Claessen, *Phys. Rev. B* **2018**, *97*, 075101.
[32] A. A. Baker, A. I. Figueroa, D. Pingstone, V. K. Lazarov, G. van der Laan, T. Hesjedal, *Sci. Rep.* **2016**, *6*, 35582.
[33] Ł. Gladczuk, L. Gladczuk, P. Dluzewski, G. van der Laan, T. Hesjedal, *Phys. Stat. Solidi - Rapid Res. Lett.* **2021**, *15*, 2100137.
[34] K. Eberl, W. Wegscheider, G. Abstreiter, *J. Crys. Growth* **1991**, *111*, 882.
[35] R. F. C. Farrow, D. S. Robertson, G. M. Williams, A. G. Cullis, G. R. Jones, I. M. Young, P. N. J. Dennis, *J. Cryst. Growth* **1981**, *54*, 507.
[36] I. Madarevic, U. Thupakula, G. Lippertz, N. Claessens, P.-C. Lin, H. Bana, S. Gonzalez, G. Di Santo, L. Petaccia, M. N. Nair, L. M. Pereira, C. Van Haesendonck, M. J. Van Bael, *APL Mater.* **2020**, *8*, 031114.
[37] D. T. Wang, N. Esser, M. Cardona, J. Zegenhagen, *Surf. Sci.* **1995**, *343*, 31.

[38] J. T. Ryu, M. Katayama, K. Oura, *Surf. Sci.* **2002**, *515*, 199.
[39] B. R. Cuenya, M. Doi, W. Keune, *Surf. Sci.* **2002**, *506*, 33.
[40] W. Tu, Ph.D. thesis, University of Tennessee **2014**.
[41] M. Jäger, C. Brand, A. P. Weber, M. Fanciulli, J. H. Dil, H. Pfnür, C. Tegenkamp, *Phys. Rev. B* **2018**, *98*, 165422.
[42] T. Ichikawa, *Surf. Sci.* **1984**, *140*, 37.
[43] F. Ronci, S. Colonna, A. Cricenti, G. L. Lay, *J. Phys.: Condens. Matter* **2010**, *22*, 264003.
[44] R. Cortés, A. Tejeda, J. Lobo-Checa, C. Didiot, B. Kierren, D. Malterre, J. Merino, F. Flores, E. G. Michel, A. Mascaraque, *Phys. Rev. B* **2013**, *88*, 125113.
[45] W. Srour, A. Tejeda, M. Stoffel, M. Abuín, Y. Fagot-Revurat, P. L. Fèvre, A. Taleb-Ibrahimi, D. Malterre, *J. Electron. Spectrosc. Relat. Phenom.* **2014**, *195*, 174.
[46] B. F. Mason, B. R. Williams, *Surf. Sci.* **1992**, *262*, 169.
[47] A. Barfuss, L. Dudy, M. R. Scholz, H. Roth, P. Höpfner, C. Blumenstein, G. Landolt, J. H. Dil, N. C. Plumb, M. Radovic, A. Bostwick, E. Rotenberg, A. Fleszar, G. Bihlmayer, D. Wortmann, G. Li, W. Hanke, R. Claessen, J. Schäfer, *Phys. Rev. Lett.* **2013**, *111*, 157205.
[48] T. Osaka, H. Omi, K. Yamamoto, A. Ohtake, *Phys. Rev. B* **1994**, *50*, 7567.
[49] L. Gladczuk, P. Aleshkevych, R. Szymczak, P. Dluzewski, M. Aleszkiewicz, W. Paszkowicz, R. Minikayev, P. Przyslupski, *J. Appl. Phys.* **2009**, *105*, 063907.
[50] A. N. Bogdanov, I. E. Dragunov, *Low Temp. Phys.* **1998**, *24*, 852.
[51] Ł. Gladczuk, Ph.D. thesis, University of Oxford **2021**.
[52] D. R. Lide, *Handbook of Chemistry and Physics*, CRC Press, Boca Raton **1992**.
[53] L. Gladczuk, P. Aleshkevych, K. Lasek, P. Przyslupski, *J. Appl. Phys.* **2014**, *116*, 233909.
[54] Ł. Gladczuk, L. Gladczuk, P. Dluzewski, K. Lasek, P. Aleshkevych, D. M. Burn, G. van der Laan, T. Hesjedal, *Phys. Rev. B* **2021**, *103*, 064416.